



Airfoil Thickness Effects on Dynamic Stall Onset

Anupam Sharma*

Department of Aerospace Engineering, Iowa State University, Ames, IA, USA, 50011.

and

Miguel Visbal†

Computational Sciences Center, Air Force Research Laboratory, Wright-Patterson AFB, OH 45433.

Large eddy simulations are used to investigate the effects of airfoil geometry, particularly thickness, on inception of dynamic stall. The investigation is performed for three airfoils from the NACA family at $Re_c = 2 \times 10^5$. Three symmetric airfoils are studied with thickness-to-chord ratios of 9%, 12%, and 15%. A constant-rate pitch-up motion about the airfoil quarter-chord point is used to study dynamic stall. A static simulation is first carried out with each airfoil set at $\alpha = 4^\circ$. Results of the static simulations are compared with XFOIL predictions as a sanity check. Good code-to-code agreement is observed for aerodynamic pressure- and skin friction coefficient distributions. A ramp function is used to smoothly increase the pitch rate from zero to the desired value and then held fixed. Dynamic simulations are carried out until the angle of attack goes past the lift stall point. Unsteady aerodynamic loads are compared with the corresponding static values. In all cases, dynamic stall onset occurs immediately following the bursting of the laminar separation bubble. However, investigation of the reverse flow region on the suction surface shows tremendous differences between the different airfoils, with the thickest airfoil showing a very large reverse flow region. These observations suggests that the mechanism of stall onset can change from ‘LSB burst’ to trailing edge separation as airfoil thickness is further increased.

I. Introduction

UNSTEADY flow over streamlined surfaces such as aircraft wings and helicopter (or wind turbine) rotor blades produces interesting but usually undesirable phenomena such as flutter, buffeting, gust response, and dynamic stall.¹ Dynamic stall is a nonlinear fluid dynamics phenomenon that occurs frequently on rapidly maneuvering aircraft,² helicopter rotors,³ and wind turbines,^{4,5} and is characterized by large increases in lift, drag, and pitching moment far beyond the corresponding static stall values. Carr⁶ presents an excellent review on dynamic stall. Dynamic stall can be divided into two categories based on the degree to which the angle of attack, α increases beyond the static-stall value. Denoting the maximum α reached during the unsteady motion by α_{max} , these categories are: (1) *Light stall*: when α_{max} is small, the viscous, separated flow region is small (of the order of the airfoil thickness), and (2) *Deep stall*: for large α_{max} , the viscous region becomes comparable to the airfoil chord. A prominent feature of deep stall is the presence of the dynamic stall vortex (DSV) that is primarily responsible for the large overshoots in aerodynamic forces and moments.

Many fundamental aspects of flutter, buffeting, and gust response can be explained using linearized theory. Pioneering work in this area was done by Theodorsen⁷ and Karman and Sears.⁸ Their application however is limited to small perturbations and the highly nonlinear phenomenon of dynamic stall is beyond their reach. Semi-empirical methods^{9,10} have also been developed to model dynamic stall. These methods are invaluable for preliminary design and analysis, but they do not provide insight into the physical mechanisms. Computational investigations have included Reynolds Averaged Navier-Stokes (RANS) computations¹¹ and large eddy simulations (LES).^{12,13} Recent computational efforts have focused on using highly resolved LES to investigate dynamic stall on flat plates¹² and airfoils.¹¹ All of these simulations have focused on relatively

*Assistant Professor, 2341 Howe Hall, Ames, IA, 50011. sharma@iastate.edu. AIAA Senior Member.

†Principal Research Aerospace Engineer, miguel.visbal@us.af.mil

thin airfoils operating at low-to-moderate Reynolds numbers, $10^4 < Re_c < 5 \times 10^5$. In this paper, we explore the effects of airfoil geometry, particularly thickness, on the onset of dynamic stall.

II. Methodology

The extensively validated compressible Navier-Stokes solver, FDL3DI¹⁴ is used for the fluid flow simulations. FDL3DI solves the full, unfiltered Navier-Stokes equations on curvilinear meshes. The solver can work with multi-block overset (Chimera) meshes with high order interpolation methods that extend the spectral-like accuracy of the solver to complex geometries. The solver can be run in a large eddy simulation (LES) mode with the effect of sub-grid stresses (SGS) modeled implicitly using spatial (low-pass) filtering to remove the energy at the unresolved scales. *Discriminating*, high-order, low-pass spatial filters are implemented that regularize the procedure without excessive dissipation.

A. Governing Equations

The governing fluid flow equations (solved by FDL3DI), after performing a time-invariant curvilinear coordinate transform from physical coordinates $(x, y, z) \rightarrow$ to computational coordinates (ξ, η, ζ) , are written in a strong conservation form as

$$\frac{\partial}{\partial t} \left(\frac{\mathbf{Q}}{J} \right) + \frac{\partial \hat{\mathbf{F}}_I}{\partial \xi} + \frac{\partial \hat{\mathbf{G}}_I}{\partial \eta} + \frac{\partial \hat{\mathbf{H}}_I}{\partial \zeta} = \frac{1}{Re} \left[\frac{\partial \hat{\mathbf{F}}_v}{\partial \xi} + \frac{\partial \hat{\mathbf{G}}_v}{\partial \eta} + \frac{\partial \hat{\mathbf{H}}_v}{\partial \zeta} \right], \quad (1)$$

where $J = \partial(\xi, \eta, \zeta, \tau)/\partial(x, y, z, t)$ is the Jacobian of the coordinate transformation, $\mathbf{Q} = \{\rho, \rho u, \rho v, \rho w, \rho E\}$; the inviscid flux terms, $\hat{\mathbf{F}}_I, \hat{\mathbf{G}}_I, \hat{\mathbf{H}}_I$ are

$$\hat{\mathbf{F}}_I = \begin{bmatrix} \rho \hat{U} \\ \rho u \hat{U} + \hat{\xi}_x p \\ \rho v \hat{U} + \hat{\xi}_y p \\ \rho w \hat{U} + \hat{\xi}_z p \\ (\rho E + p) \hat{U} - \hat{\xi}_t p \end{bmatrix}, \quad \hat{\mathbf{G}}_I = \begin{bmatrix} \rho \hat{V} \\ \rho v \hat{V} + \hat{\eta}_x p \\ \rho v \hat{V} + \hat{\eta}_y p \\ \rho w \hat{V} + \hat{\eta}_z p \\ (\rho E + p) \hat{V} - \hat{\eta}_t p \end{bmatrix}, \quad \text{and} \quad \hat{\mathbf{H}}_I = \begin{bmatrix} \rho \hat{W} \\ \rho u \hat{W} + \hat{\zeta}_x p \\ \rho v \hat{W} + \hat{\zeta}_y p \\ \rho w \hat{W} + \hat{\zeta}_z p \\ (\rho E + p) \hat{W} - \hat{\zeta}_t p \end{bmatrix}, \quad (2)$$

where,

$$\begin{aligned} \hat{U} &= \hat{\xi}_t + \hat{\xi}_x u + \hat{\xi}_y v + \hat{\xi}_z w, \\ \hat{V} &= \hat{\eta}_t + \hat{\eta}_x u + \hat{\eta}_y v + \hat{\eta}_z w, \\ \hat{W} &= \hat{\zeta}_t + \hat{\zeta}_x u + \hat{\zeta}_y v + \hat{\zeta}_z w, \quad \text{and} \\ \rho E &= \frac{p}{\gamma - 1} + \frac{1}{2} \rho (u^2 + v^2 + w^2). \end{aligned} \quad (3)$$

In the above, $\hat{\xi}_{(x,y,z)} = J^{-1} \partial \xi / \partial (x, y, z)$, and u, v, w are the components of the velocity vector in Cartesian coordinates, and ρ, p, T are respective the fluid density, pressure, and temperature. The gas is assumed to be perfect, $p = \rho T / \gamma M_\infty^2$. The viscous flux terms, $\hat{\mathbf{F}}_v, \hat{\mathbf{G}}_v, \hat{\mathbf{H}}_v$ are provided in Ref.¹⁵

III. Meshing

The simulations are carried out at a chord-based Reynolds number, $Re_c = 200,000$ and a flow Mach number, $M_\infty = 0.1$. The span length of the airfoil model in the simulations is 10% of the airfoil chord. The first cell height is selected to obtain a $y^+ \approx 0.2$. A planar, single-block O-mesh is generated around the airfoil, which is repeated with uniform grid spacing in the span direction. The mesh is highly refined over the suction side to resolve the viscous flow phenomena expected during the airfoil pitch up motion. The boundary layer on the pressure side remains attached and primarily laminar through the course of the simulations. A relatively coarse mesh is therefore sufficient to discretize the pressure side.

The O-grid in the physical space (x, y, z) maps to an H-grid in the computational domain (ξ, η, ζ) . The following orientation is used: \hat{e}_ξ points radially out, \hat{e}_η is in the circumferential direction, and \hat{e}_ζ is along the span direction such that the right hand rule, $\hat{e}_\zeta = \hat{e}_\xi \times \hat{e}_\eta$ is obeyed.

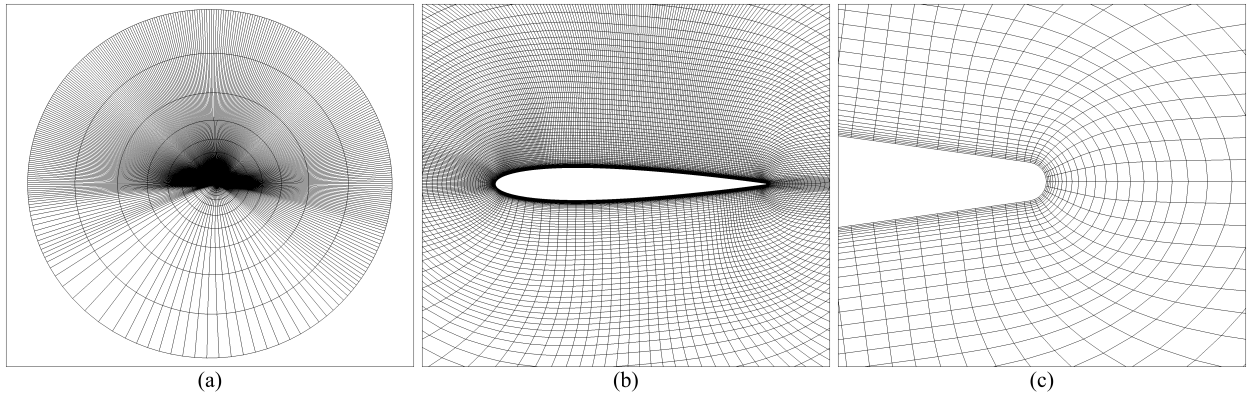


Figure 1. Three views of the mesh used for the NACA 0012 simulation: (a) full computational domain, (b) zoom view of the grid around the airfoil, and (c) zoom view showing the trailing edge geometry and resolution. Every fifth- and every fourth point in the radial and circumferential directions respectively are shown for clarity.

Periodic boundary conditions on the η boundaries simulate the continuity in the physical space around the airfoil. Periodicity is also imposed at the boundaries in the span direction (\hat{e}_ζ). Periodic boundary conditions are implemented using the Overset grid approach in FDL3DI. A minimum of five-point overlap is required by the FDL3DI solver to ensure high-order accurate interpolation between individual meshes. A five-point overlap is therefore built into the mesh. Similar overlaps are created automatically in FDL3DI between blocks when domain decomposition is used to split each block into multiple sub-blocks for parallel execution.

The simulations are performed in two steps. In the first step, a statistically stationary solution is obtained with the airfoil set at angle of attack, $\alpha = 4^\circ$; this is referred to as ‘static’ simulation. Dynamic simulations with airfoil motion are simulated in the second step. A constant-rate, pitch-up motion is prescribed with the pitching axis located at the quarter-chord point of the airfoil.

A. Mesh Sensitivity Study

A mesh sensitivity study is performed where dependence of the results on grid size is evaluated for both static and dynamic simulations. Three mesh sizes are evaluated. The overall grid dimensions and non-dimensional cell sizes (average and maximum values) for the different meshes are provided in Table 1. The non-dimensional cell sizes are evaluated using the static simulations of NACA-0012 airfoil performed at $\alpha = 4^\circ$.

Table 1. Grid dimensions and non-dimensional cell sizes. Mesh dimensions are listed as $N_\xi \times N_\eta \times N_\zeta$.

Grid	dimensions	y^+ (avg, max)	x^+ (avg, max)	z^+ (avg, max)
Coarse	$395 \times 643 \times 51$	0.36, 0.94	22.0, 55.1	17.0, 63.9
Medium	$410 \times 995 \times 101$	0.18, 0.47	14.3, 85.2	8.5, 32.4
Fine	$410 \times 1341 \times 134$	0.19, 0.50	10.6, 87.2	7.0, 24.5

Aerodynamic pressure coefficient and skin friction coefficient for the static simulations are compared between the three grids in Fig. 2. All three grids capture the transition location (at $x/c \approx 0.45$) on the suction surface, which is triggered in the shear layer formed due to the laminar separation. The turbulent boundary layer then reattaches to the surface forming a laminar separation bubble (LSB). The Coarse grid shows a slightly shorter LSB as seen by inspecting the C_f plot (Fig. 2 b). Furthermore, the Medium and Fine grids show an extended transition region as compared to the Coarse grid. The Medium and Fine grids show very comparable results.

The time step for the dynamic simulations is kept fixed at 2×10^{-5} units for all three grids. The airfoil is pitched up at a constant rate from $\alpha = 4^\circ$ until lift stall occurs. Figure 3 (a,b) compares the predicted

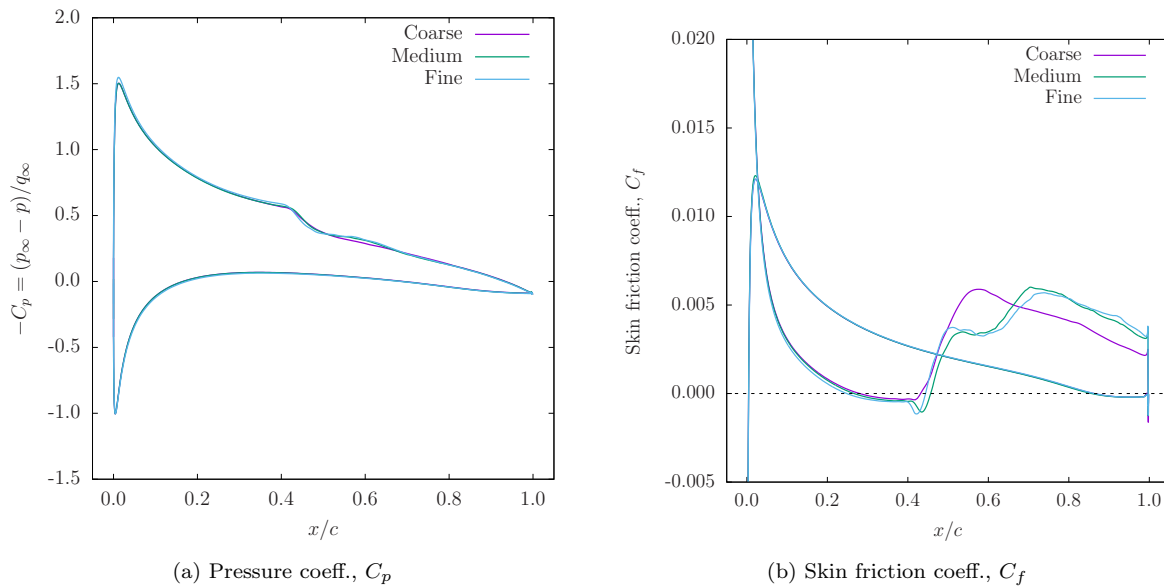


Figure 2. Results of static simulations to investigate mesh sensitivity.

histories of lift and drag coefficients for the three grids. The differences between the Coarse grid and the other two grids are more apparent in the dynamic simulation results. Dynamic stall does not begin until $\alpha = 24^\circ$ with the Coarse grid, whereas stall onset is observed at around $\alpha = 17^\circ$ for the Medium and Fine grids. The Medium and Fine grids exhibit very similar time histories for C_l and C_d . Figure 3 (c,d,e) plots the C_p distribution over the suction surface of the airfoil. The streak of large negative C_p that moves downstream as α is increased is associated with the dynamic stall vortex (DSV). The formation of the DSV is significantly delayed in the Coarse grid simulation, whereas the Medium and Fine grid results show converged results. Based on this study, the Fine grid is selected for the simulations with cell counts in the radial, circumferential, and spanwise directions equal to 410, 1341, and 134 respectively, giving a total cell count of about 74 million.

IV. Results

This section presents the results of the static and dynamics simulations. The FDL3DI results for the static simulations are compared with XFOIL results as a sanity check.

A. Static Simulations

For the static simulations, the x axis of the coordinate system is aligned with the airfoil chord and a uniform inflow velocity is prescribed at the desired angle of attack ($\alpha = 4^\circ$ here). The simulation is started with a potential flow solution as the initial condition and carried out until statistical convergence is obtained. Statistical convergence is checked for integrated airfoil loads, as well as for static pressure at a few point probes placed in the suction side boundary layer. Surface properties, such as aerodynamic pressure coefficient (C_p) and skin friction coefficient (C_f) are extracted from the time-averaged data.

Figure 4 compares the FDL3DI predicted C_p and C_f distributions against those obtained using XFOIL for the NACA-0015 airfoil. The XFOIL simulations are performed with the N_{crit} parameter set equal to 11. N_{crit} is the log of the amplification factor of the most-amplified wave that triggers transition. A value of 11 for N_{crit} is appropriate for use with airfoil models tested in a “clean” wind tunnel (i.e., with very low inflow turbulence). Since the inflow in FDL3DI simulations is uniform with zero turbulence, $N_{crit} = 11$ is deemed appropriate. The overall agreement between XFOIL and FDL3DI is good.

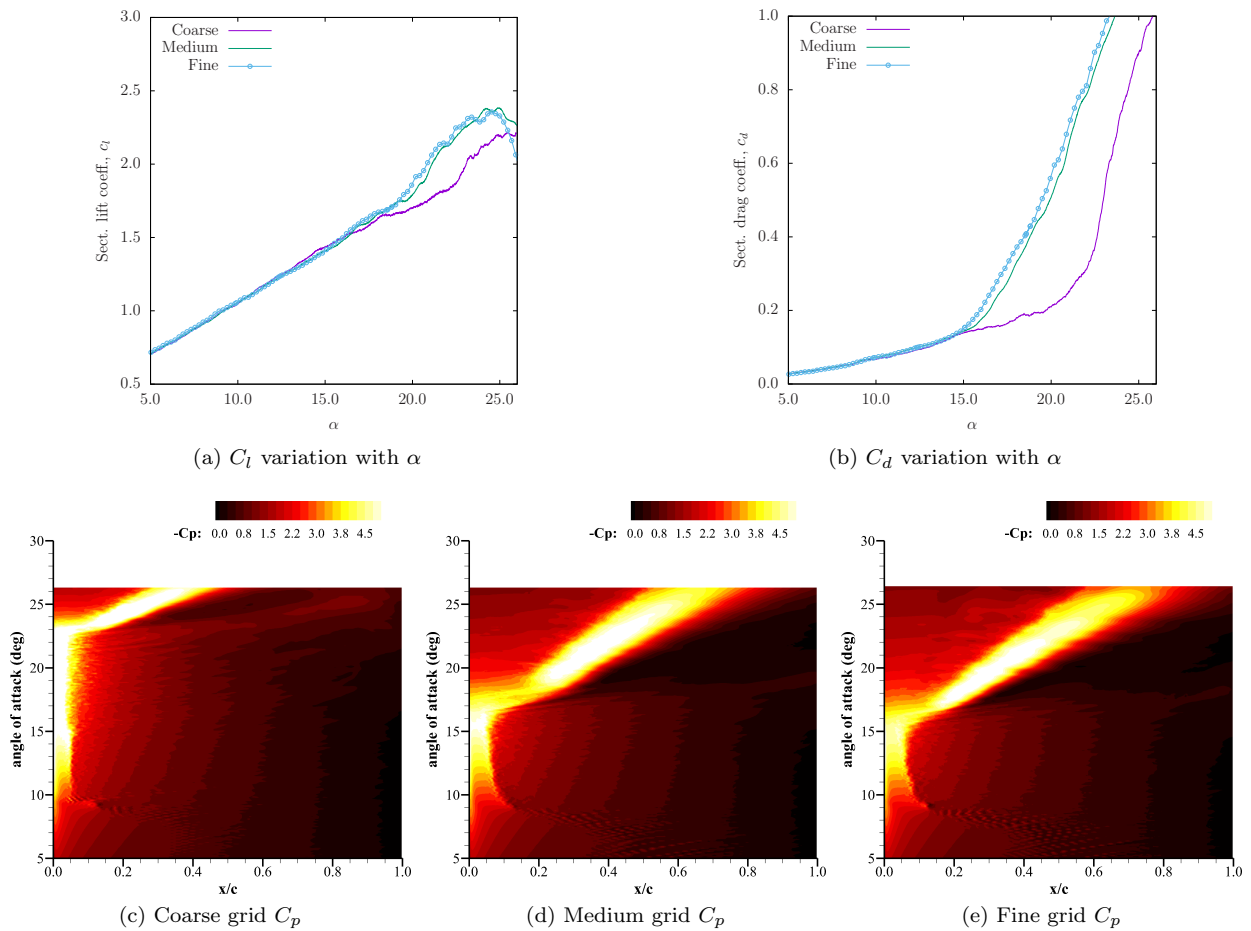


Figure 3. Results of dynamic simulations to investigate mesh sensitivity. Plots (a) and (b) show airfoil sectional lift and drag coefficients as functions of angle of attack, α . Plots (c), (d), and (e) show variation of $-C_p$ with α over the suction side of the airfoil. The DSV formation occurs at much higher α in the Coarse grid simulation.

B. Dynamic Simulations

In the second step, the airfoil pitch-up motion is simulated via grid motion. A constant-pitch rate motion, with the pitching axis located at the airfoil quarter-chord point, is investigated. The non-dimensional rotation (pitch) rate is $\Omega_0^+ = \Omega_0 c / u_\infty = 0.05$. The ramp function defined by Eq. 4 is used to smoothly transition $\Omega^+(t)$ from zero at $t = 0$ to Ω_0^+ at $t = t_0$. Beyond t_0 , the airfoil continues to pitch at $\Omega_0^+ = 0.05$, with the angle of attack increasing linearly with the pitch angle.

$$\Omega^+(t) = \frac{\Omega_0^+}{2} \left(\frac{\tanh(s(2t/t_0 - 1))}{\tanh(s/t_0)} + 1 \right) \quad (4)$$

The different flow stages experience by the airfoil during this prescribed dynamic motion are summarized below in chronological order:

1. The transition location on the suction surface moves upstream.
2. The laminar separation bubble (LSB) on the suction surface moves upstream and reduces in size as the airfoil is pitched.
3. Collapse of the suction peak occurs as the LSB bursts. This is followed immediately by the development of a dynamic stall vortex (DSV).
4. As the DSV convects downstream, the shear layer in the aft portion of the airfoil rolls up into a shear layer vortex (SLV).

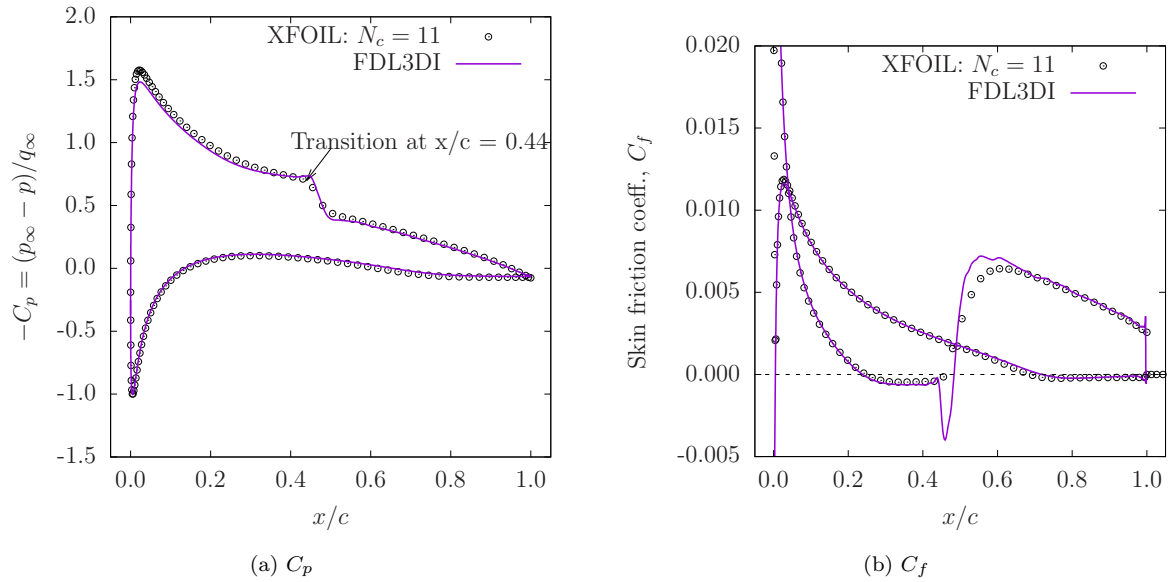


Figure 4. Comparison of coefficient of pressure, C_p and skin friction coefficient, C_f between predictions by FDL3DI and XFOIL for NACA-0015 airfoil. XFOIL is run with $N_{crit} = 11$ to simulate very low inflow turbulence.

5. The airfoil pitch-down moment ($-C_M$) increases sharply, and moment stall occurs.
6. Lift stall occurs when the additional lift due to the sudden drop in the induced velocity as the DSV reaches the airfoil TE.

These sequence of events can be seen in the snapshots of the predicted flowfield for the NACA-0012 airfoil. Each plot in Fig. 5 shows the iso-surfaces of the Q-criterion colored by the value of the x -component of flow velocity. All the airfoils tested here follow the same general pattern as the pitch angle is increased through stall, although there are differences in unsteady lift increase, local pressure peaks, and amount of trailing edge separation.

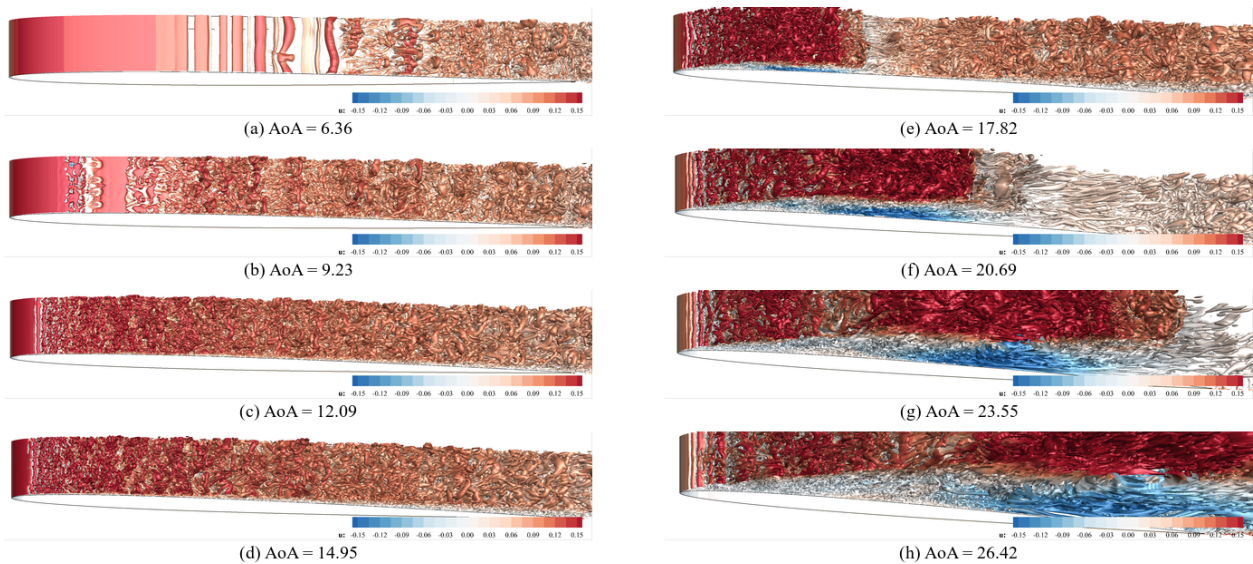


Figure 5. Iso-surfaces of Q-criterion with colored contours of x -component of flow velocity of the NACA-0012 simulation at various stages of dynamic stall.

1. Lift, Drag, and Moment Variations

Figure 6 compares the dynamic section lift-, drag-, and moment coefficients for the three simulated airfoils as they undergo the constant-rate pitching motion. We focus first on the NACA-0012 simulation. The slope of the $C_l - \alpha$ curve increases around $\alpha = 18^\circ$, which is due to the strengthening of the DSV and the associated increase in lift. This is immediately followed by moment stall, marked by the strong divergence in the $C_m - \alpha$ curve. The sharp increase in the pitch-down moment is due to the progressive aft propagation of the loading induced by the DSV. At around $\alpha = 25^\circ$ the DSV reaches close to the trailing edge and away from the airfoil. As a result the lift induced by the DSV reduces dramatically and lift stall occurs.

Comparing the lift and moment curves for the three airfoils (see Fig. 6) shows that the NACA-0009 airfoil experiences the largest increase in lift and moment due to airfoil motion (dynamic stall), while the NACA-0015 experiences the smallest. The increase in unsteady lift is measured as the difference of $C_{l,max}$ between dynamic- and static stall. The dynamic stall values are obtained using FDL3DI while the static values are obtained using XFOIL (not shown). While unsteady loads reduce with increasing airfoil thickness, stall delay (as measured by the difference in α where dynamic stall occurs versus where static stall occurs) remains nearly unchanged.

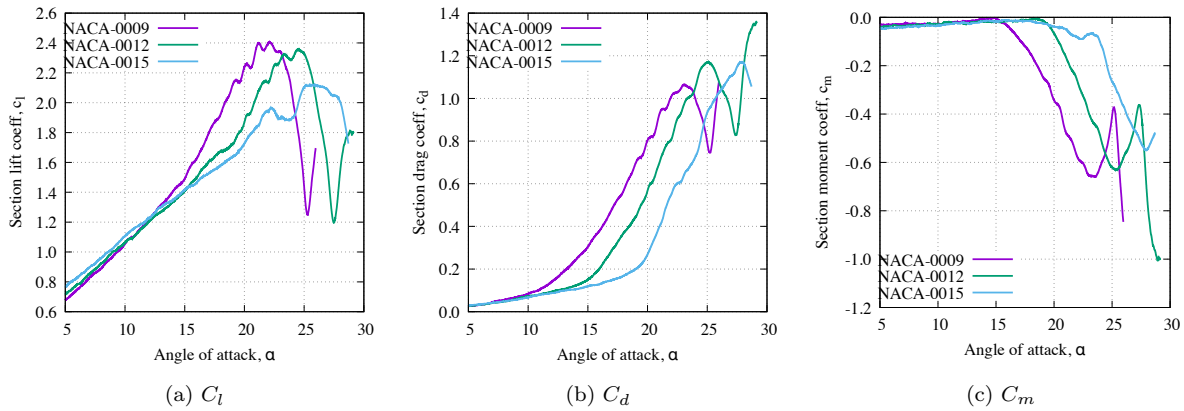


Figure 6. Section lift-, drag-, and moment coefficients as functions of angle of attack during a constant pitch-rate maneuver.

Table 2. Angle of attack values at which static stall and dynamic stall occurs for different airfoils.

	Moment Stall	Lift Stall		
	$\alpha_{DS}^{(M)}$	$\alpha_{DS}^{(L)}$	$\alpha_{SS}^{(L)}$	$\Delta\alpha^{(L)} = \alpha_{DS}^{(L)} - \alpha_{SS}^{(L)}$
NACA 0009	15.0	22.2	10.7	11.5
NACA 0012	18.7	24.6	13.7	10.9
NACA 0015	23.5	25.5	15.0	10.5

2. Onset of Dynamic Stall

McCroskey *et al.*¹⁶ classifies dynamic stall into the following categories:

1. *Leading edge stall:* It can occur due to (a) bursting of the LSB as the adverse pressure gradient increases beyond a threshold, and the separated shear layer does not re-attach to the airfoil surface, or due to (b) reverse flow region abruptly propagating upstream all the way to the leading edge of the airfoil.
2. *Trailing edge stall:* The reverse flow region near the airfoil trailing edge gradually expands as the airfoil is pitched up. As the flow separation location moves upstream and reaches close to the leading edge, the dynamic stall vortex (DSV) forms and stall occurs.
3. *Thin airfoil stall:* When the LSB gradually becomes bigger in size and covers the entire airfoil, leading to stall, it is referred to as thin airfoil stall.

4. *Mixed stall*: Mixed stall is said to occur if either (a) the flow separates both at the leading and trailing edges of the airfoil at the same time and the separation progress toward the middle of the airfoil from both ends, or (b) flow separates in the middle of the airfoil followed by one separation branch moving upstream and the other downstream.

We investigate the mechanism of stall onset for the cases considered here by analyzing the details of the flowfield over the suction surface for each airfoil. Figures 7 and 8 respectively plot spanwise averaged contours of $-C_p$ and C_f (denoted by $-\langle C_p \rangle$ and $\langle C_f \rangle$ respectively) on the suction side of the airfoil as functions of chordwise distance and angle of attack, α . This representation is similar to $x-t$ diagrams with α representing time (t) scaled by the pitch rate (since the pitch rate is constant). $x-t$ diagrams are useful to identify characteristics of hyperbolic equations. Contour plots are shown for all four cases. The sequence of flow events identified earlier in Section B are clearly seen in the contour plots. The transition location is identified by the boundary where the 2D instability modes (seen clearly in Fig. 8 as alternating blue and red spots) start to appear. The transition location moves upstream with increasing α . The speed at which the transition location moves upstream reduces with increasing airfoil thickness. The LSB forms near the leading edge and is sustained up to approximately $\alpha = 11^\circ$, 15° , and 19° for the 9%, 12%, and 15% thick airfoils respectively.

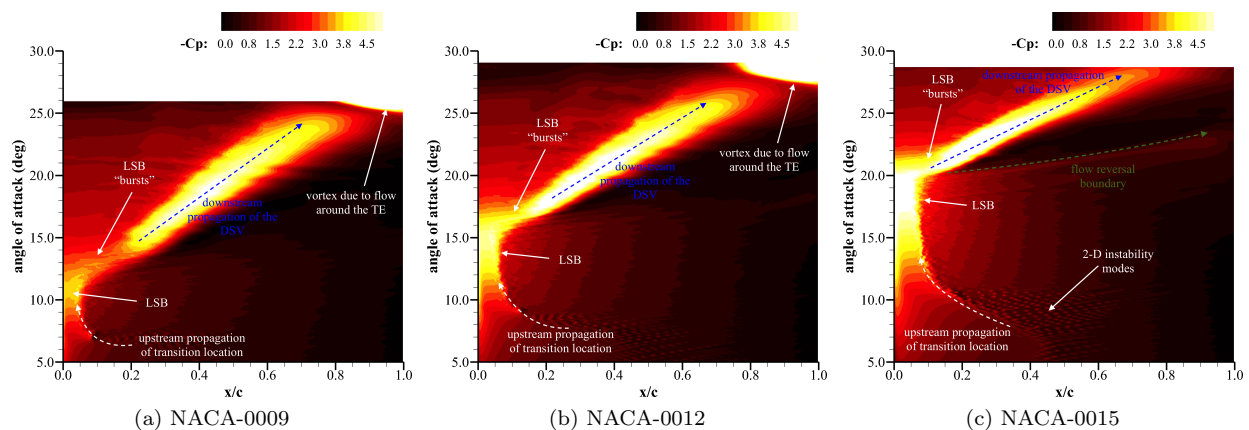


Figure 7. Contours of span-averaged pressure coefficient ($\langle C_p \rangle$) on the suction side of the four airfoils through the constant-rate pitch-up motion.

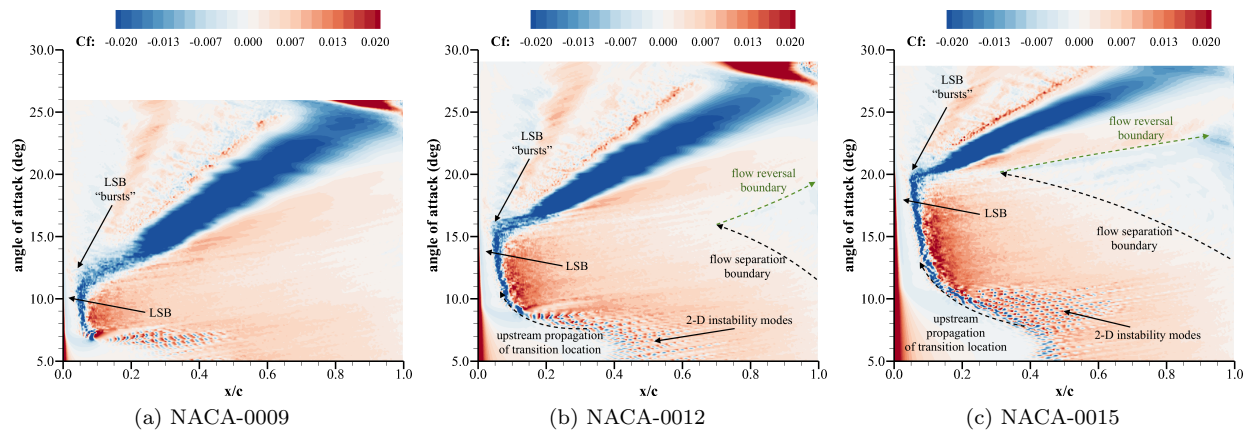


Figure 8. Contours of span-averaged skin friction coefficient ($\langle C_f \rangle$) on the suction side of the four airfoils through the constant pitch-rate motion.

Figure 9 plots instantaneous contours of chordwise blade relative velocity for each airfoil immediately prior to onset of dynamic stall. The contours are cutoff above the zero value to show only the reverse flow regions. Reverse flow region is clearly visible in the aft portion of the relatively thick airfoils (NACA-0015 and NACA-0018), while the 9% and 12% thick airfoils show almost no flow reversal. While these plots

provided a good qualitative view of how far upstream the reverse flow region reaches at the onset of dynamic stall, the skin friction coefficient is examined next for a quantitative assessment.

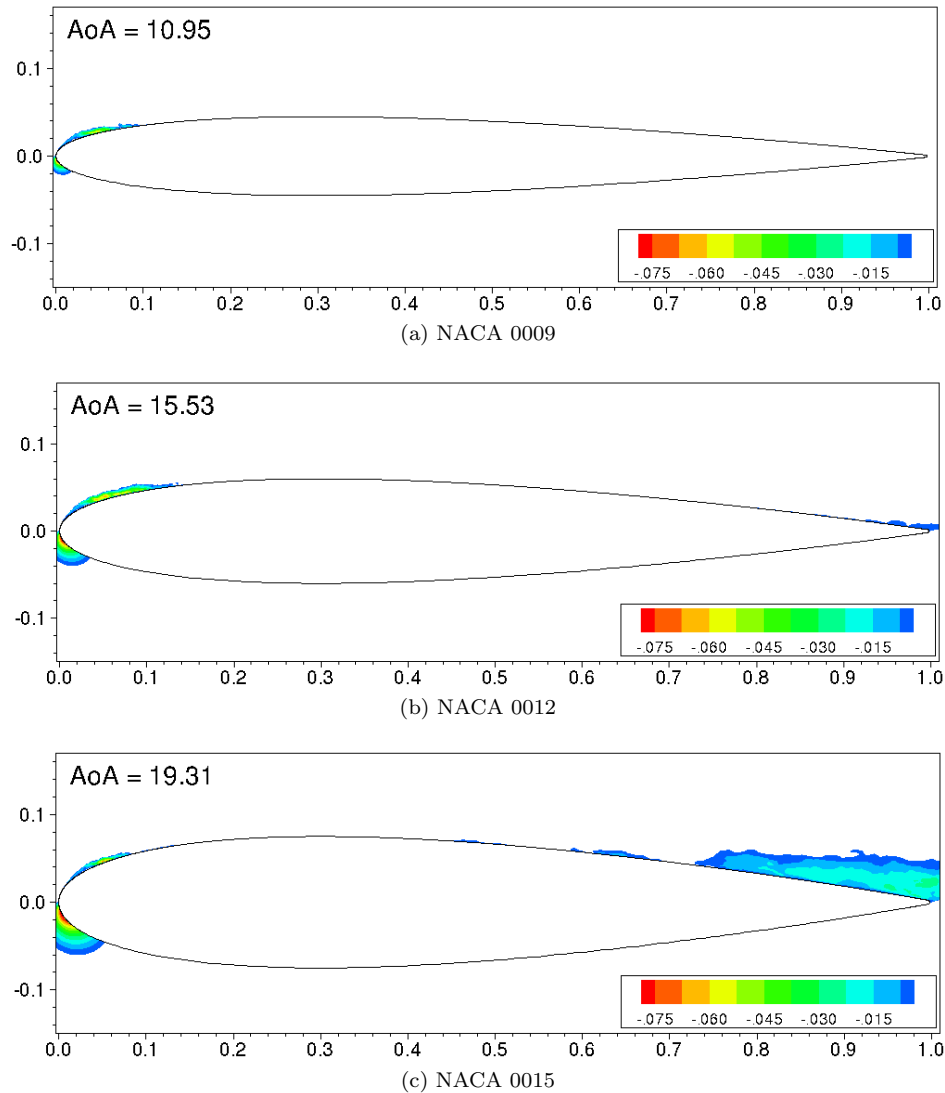


Figure 9. Contours of blade-relative chord-wise flow velocity immediately before onset of dynamic stall. The contours are cut-off above 0 to identify reverse flow regions.

Figure 10 shows line plots of $-\langle C_p \rangle$ and $\langle C_f \rangle$ along the NACA-0015 airfoil chord at five different angles of attack (α) during the pitch-up maneuver. The α values are selected to illustrate a few interesting stages in the pitch up maneuver. At $\alpha = 9.23^\circ$, the laminar boundary layer over the airfoil separates locally (see $\langle C_f \rangle$ plot) and transitions; the transition region shows oscillations corresponding to the instability modes in both $\langle C_p \rangle$ and $\langle C_f \rangle$. At $\alpha = 13.81^\circ$, the LSB is securely positioned close to the airfoil leading edge and the boundary layer transitions abruptly right behind the LSB. Some evidence of the turbulent boundary layer separating near the trailing edge is also visible. Further increase in α to 19.31° causes the LSB to move upstream and shrink in size. At this time, the turbulent boundary layer is separated beyond mid-chord ($\langle C_f \rangle < 0$). The LSB bursts as α is increased beyond 19.31° and the DSV forms. The DSV is seen as locally increased C_p value in the curves for $\alpha = 20.69^\circ$ and 22.98° . As the DSV forms and convects downstream, some part of the turbulent boundary layer reattaches (as seen in the C_f curve for $\alpha = 22.98^\circ$) due to the large induced velocity by the DSV. This is marked as “flow reversal boundary” in Figs. 7 and 8.

Figure 11 compares C_f distributions between the three airfoils taken immediately prior to the bursting of the LSB. No flow separation is seen near the trailing edge for the thinnest airfoil. The NACA-0012 simulation shows reverse flow in a very small region near the trailing edge, while more than 50% of the NACA-0015

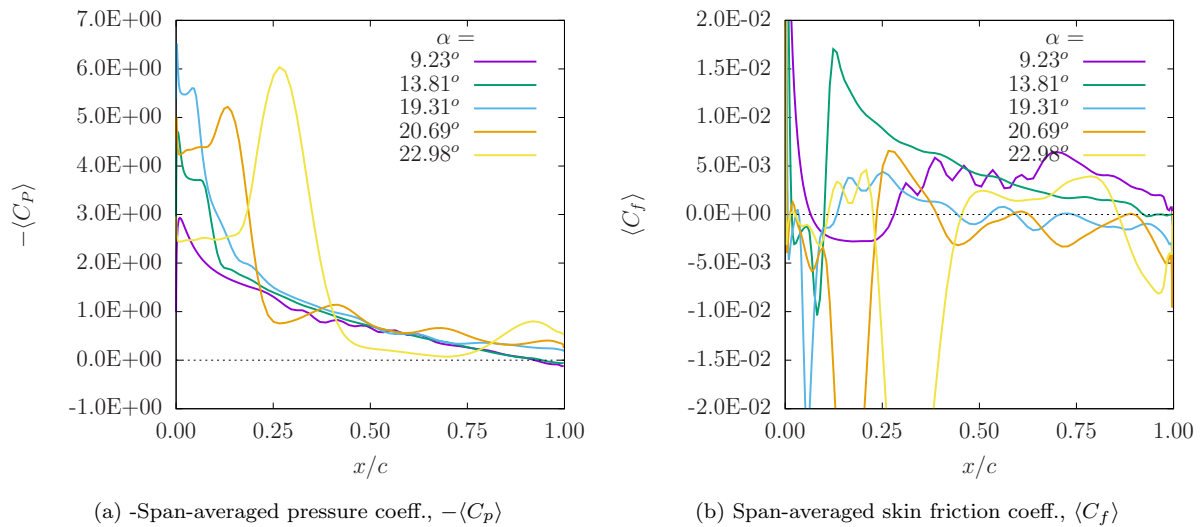


Figure 10. Distributions of $-\langle C_p \rangle$ and $\langle C_f \rangle$ along the NACA-0015 chord at five angles of attack during the pitch up maneuver.

airfoil experiences reverse flow before LSB burst.

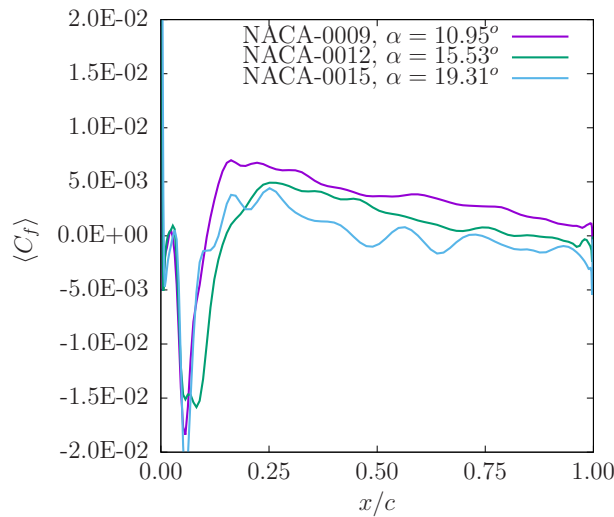


Figure 11. $\langle C_f \rangle$ distributions on the suction surfaces of the four airfoils immediately before onset of dynamic stall.

V. Conclusions

Onset of dynamic stall is investigated at $Re_c = 2 \times 10^5$ for three symmetric NACA airfoils of varying thickness - 9%, 12%, and 15%. A constant rate pitch-up airfoil motion about the quarter-chord point is investigated using wall-resolved large eddy simulations. Comparisons are drawn against XFOIL for static simulations at angle of attack, $\alpha = 4^\circ$. Overall, the agreement between FDL3DI and XFOIL in predicting C_p and C_f distributions is good.

Dynamic simulations show the following sequence of events: (1) upstream movement of the transition location, (2) formation of a laminar separation bubble (LSB) and rise in suction peak pressure, (3) LSB burst followed by formation of the dynamic stall vortex (DSV), (4) roll-up of boundary layer vorticity into a shear layer vortex, (5) sharp increase in pitch-down moment (moment stall), and (5) precipitous drop

in airfoil lift (lift stall). While all the airfoils undergo the same sequence of events, the duration of each event and the associated aerodynamics differ substantially with airfoil thickness. The thinnest airfoil tested (NACA-0009) experiences the largest increase in sectional lift coefficient whereas the highest peak suction pressure is obtained for the thickest airfoil.

Investigation of skin friction coefficient on the suction surface shows that while turbulent boundary layer separation is nearly non-existent for NACA-0009, the separation (flow reversal) region for the thickest airfoil spans a large portion of the airfoil. This observation suggests that stall onset could be triggered by the turbulent separation region reaching up to the LSB for an even thicker airfoil. The mechanism of stall onset can therefore gradually change with increasing airfoil thickness from that due to LSB burst to trailing edge stall.

Acknowledgments

Funding for this research is provided by the AFOSR Summer Faculty Fellowship program and by the National Science Foundation under grant number NSF/ CBET-1554196. Computational resources are provided by NSF XSEDE (Grant #TG-CTS130004) and the Argonne Leadership Computing Facility, which is a DOE Office of Science User Facility supported under Contract DE-AC02-06CH11357.

The second author would like to acknowledge support by AFOSR under a task monitored by Dr. D. Smith, and by a grant of HPC time from the DoD HPC Shared Resource Centers at AFRL and ERDC. Technical support for the FDL3DI software provided by Dr. Daniel Garmann of the Air Force Research Laboratory is acknowledged.

References

- ¹McCroskey, W. J., "Unsteady Airfoils," *Annual Review of Fluid Mechanics*, Vol. 14, No. 1, 1982, pp. 285–311.
- ²Brandon, J. M., "Dynamic stall effects and applications to high performance aircraft," Tech. Rep. AGARD-R-776, National Institute of Aeronautics and Astronautics, 1991.
- ³Ham, N. D. and Garelick, M. S., "Dynamic stall considerations in helicopter rotors," *Journal of the American Helicopter Society*, Vol. 13, No. 2, 1968, pp. 49–55.
- ⁴Fujisawa, N. and Shibuya, S., "Observations of dynamic stall on Darrieus wind turbine blades," *Journal of Wind Engineering and Industrial Aerodynamics*, Vol. 89, No. 2, 2001, pp. 201–214.
- ⁵Larsen, J. W., Nielsen, S. R., and Krenk, S., "Dynamic stall model for wind turbine airfoils," *Journal of Fluids and Structures*, Vol. 23, No. 7, 2007, pp. 959–982.
- ⁶Carr, L. W., "Progress in analysis and prediction of dynamic stall," *Journal of aircraft*, Vol. 25, No. 1, 1988, pp. 6–17.
- ⁷Theodorsen, T. and Mutchler, W., "General theory of aerodynamic instability and the mechanism of flutter," Report, National Aeronautics and Space Administration, 1935.
- ⁸Karman, T. v. and Sears, W. R., "Airfoil Theory of Non-Uniform Motion," *Journal of the Aeronautical Sciences*, Vol. 5, No. 10, 1938, pp. 379–390.
- ⁹Leishman, J. and Beddoes, T., "A SemiEmpirical Model for Dynamic Stall," *Journal of the American Helicopter society*, Vol. 34, No. 3, 1989, pp. 3–17.
- ¹⁰Ericsson, L. and Reding, J., "Fluid mechanics of dynamic stall part I. Unsteady flow concepts," *Journal of fluids and structures*, Vol. 2, No. 1, 1988, pp. 1–33.
- ¹¹Visbal, M. R., "Dynamic stall of a constant-rate pitching airfoil," *Journal of Aircraft*, Vol. 27, No. 5, 1990, pp. 400–407.
- ¹²Garmann, D. J. and Visbal, M. R., "Numerical investigation of transitional flow over a rapidly pitching plate," *Physics of Fluids*, Vol. 23, No. 094106, 2011.
- ¹³Visbal, M. R., "Numerical investigation of deep dynamic stall of a plunging airfoil," *AIAA journal*, Vol. 49, No. 10, 2011, pp. 2152–2170.
- ¹⁴Visbal, R. M. and Gaitonde, V. D., "On the Use of Higher-Order Finite-Difference Schemes on Curvilinear and Deforming Meshes," *Journal of Computational Physics*, Vol. 181, No. 1, 2002, pp. 155–185.
- ¹⁵Visbal, M. R. and Rizzetta, D. P., "Large-Eddy Simulation on Curvilinear Grids Using Compact Differencing and Filtering Schemes," *Journal of Fluids Engineering*, Vol. 124, No. 4, 2002, pp. 836.
- ¹⁶McCroskey, W. J., McAlister, K., Carr, L., Pucci, S., Lambert, O., and Indergrand, R., "Dynamic stall on advanced airfoil sections," *Journal of the American Helicopter Society*, Vol. 26, No. 3, 1981, pp. 40–50.